ACS APPLIED ENERGY MATERIALS

www.acsaem.org Article

Faster Diffusion and Higher Lithium-Ion Intercalation Capacity in Pb-Jarosite than Na-Jarosite

Zachary G. Neale, Michael Barta, and Guozhong Cao*

Cite This: *ACS Appl. Energy Mater.* 2021, 4, 2248−2256 Read Online

ACCESS | Metrics & More | Article Recommendations | Supporting Information

ABSTRACT: Pb-jarosite, $Pb_{0.5}Fe_3(SO_4)_2(OH)_6$, was investigated for the first time as an intercalation cathode for lithium-ion batteries. Despite having a lower theoretical specific capacity than its Na-jarosite analogue, $NaFe_3(SO_4)_2(OH)_6$, bulk Pb-jarosite displayed higher lithium-ion capacity, especially at higher current rates. The greater lithium storage is attributed to more kinetically facile diffusion of lithium in Pb-jarosite, as evidenced by potentiostatic intermittent titration technique data, indicating an average diffusion coefficient over 10 times larger. Inductively coupled plasma−optical emission spectroscopy and X-ray diffraction (XRD) measurements showed that the substitution of divalent Pb^{2+} into monovalent Na^+ sites led to an increased number of cation vacancies and a more open structure to facilitate lithium diffusion. Ex situ XRD measurements showed that Pb-jarosite is more resilient to the semireversible crystalline-to-amorphous phase transformation that occurs in Na-jarosite over many cycles. These findings demonstrate that multivalent cation substitution in jarosite materials can significantly improve their performance as intercalation cathodes.

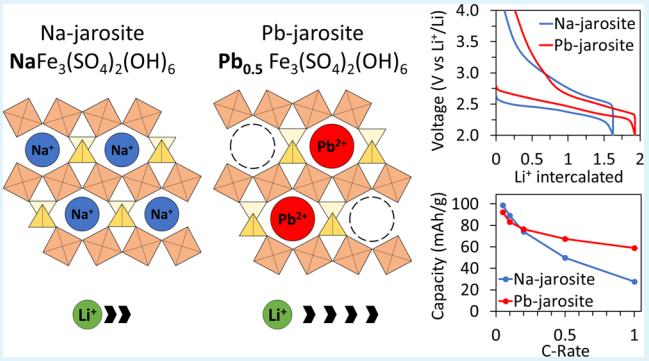

KEYWORDS: *lithium-ion battery, jarosite, diffusion, vacancies, phase transformation, crystalline-to-amorphous*

1. INTRODUCTION

The increasing demand of renewable energy and transportable electronics is coincident with development of diverse battery technologies. With increasing concerns over supply-chain stability and ethical procurement of cobalt, it is important to investigate alternative battery chemistries. Additionally, the most advanced batteries in terms of energy density may not be economically appropriate for niche roles such as residential energy storage and low-power applications. Jarosite is a natural iron-bearing mineral and waste byproduct of acid leach mining that demonstrates potential as a lithium and sodium-ion battery cathode to fill these roles.

Jarosite is a family of naturally occurring minerals that belong to the alunite supergroup with the formula $AFe_3(SO_4)_2(OH)_6$, where A represents different monovalent cations, such as K^+, Na^+, NH_4^+, and H_3O^+, or divalent cations, Pb^{2+} and Hg^{2+}.[1] The substitution of a divalent cation requires charge balance of the compound by the introduction of vacancies in A-sites. The Na-jarosite structure, $NaFe_3(SO_4)_2(OH)_6$, is built up of FeO_6 octahedra layers connected equatorially through $(OH)^-$ groups. SO_4^{2-} groups are shared between the poles of three FeO_6 and point into interlayers. The opposite poles of FeO_6 octahedra share with Na^+ 12-coordinate polyhedra which exist in between layers of FeO_6 octahedra. The substitution of monovalent Na^+ ions for divalent Pb^{2+} ions reduces the required number of 12-coordinate cations by half and introduces vacant sites, while retaining the same jarosite crystal structure.[2]

The natural jarosite ore is of little economic value; however, there has been extensive study on the formation of jarosite by mineralogists and hydrometallurgists due to its importance in the acid leach mining industry. During acid leaching of zinc, copper, and nickel-bearing ores, precipitation of jarosite in acidic media is a crucial step that allows for the physical separation of Fe^{3+} and other cations from the leach solution. As a result, these refining plants produce large amounts of environmentally hazardous jarosite wastes that are stored in containment facilities or dumped on the site.[1] These jarosite wastes currently provide no commercial value but have been the focus of research investigating the feasibility of recycling jarosite into marketable products. For example, Karamanov et al. studied the crystallization of high-iron content glass ceramics based on jarosite and several researchers have explored the use of jarosite in construction materials.[3−5]

Received: November 5, 2020
Accepted: February 22, 2021
Published: March 3, 2021

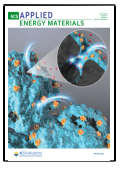

https://dx.doi.org/10.1021/acsaem.0c02762
ACS Appl. Energy Mater. 2021, 4, 2248−2256

Recycling of an environmentally hazardous waste material is an appealing aspect of jarosite and could provide it the economic advantage to make it competitive in the battery market that warrants its further investigation despite its lower energy density. Lithium and sodium intercalation into the jarosite structure was first reported by the Raveau group in 2014.[6,7] Since then, there have been several other publications on nanostructured jarosite cathodes and anodes, ammonium-jarosite, the vanadium-jarosite analogue, and fluoride-doped jarosite.[8−13] One challenge is that bulk jarosite exhibits low capacity, especially at high current rates due to slow kinetics. Currently, synthesized jarosite nanosheets and nanoparticles with short diffusion pathways provide the best capacity over many cycles and at high currents.[8,10] However, more investigation must be done on the bulk electrochemical properties of other jarosite compounds that could potentially be sourced from leach mining waste.

This study investigates the electrochemical properties of synthetic Pb-jarosite microparticles, compared to synthetic Na-jarosite. The theoretical capacities of Na-jarosite and Pb-jarosite are 166 and 142 mA h/g, respectively, when one Li^+ ion is intercalated for every Fe^{3+} cation. Although Pb-jarosite has a reduced theoretical capacity, it is hypothesized that the formation of vacancies by the substitution of divalent Pb^{2+} in place of monovalent Na^+ would increase the high-rate capability of bulk jarosite due to increased lithium-ion diffusivity.

2. EXPERIMENTAL SECTION

2.1. Synthesis of Jarosite Powders. Na-jarosite was synthesized using a precipitation procedure similar to those investigated by Dutrizac.[14] Ferric sulfate and sodium sulfate were completely dissolved in 100 mL of deionized water at concentrations of 0.1 and 0.3 M, respectively. The pH of the solution was adjusted to 1.6 at room temperature with the addition of sulfuric acid. The solution was refluxed in an oil bath at 97 °C under constant stirring for 48 h. Afterward, the yellow jarosite precipitate was collected and washed with hot deionized water and then dried at 80 °C under vacuum for 12 h.

Pb-jarosite was synthesized by preparing a 100 mL solution of 0.15 M ferric sulfate and 0.08 M lead chloride. Lead chloride did not readily dissolve into the solution due to its low solubility in water. Additionally, the solution contained 0.3 M lithium sulfate to increase the incorporation of Pb^{2+} into the product.[15] The pH was adjusted to 1.6 using sulfuric acid, and the mixture was refluxed in an oil bath at 97 °C under constant stirring for 48 h. Afterward, a yellow precipitate was collected and washed with warm 10% ammonium acetate solution in order to leach away any lead sulfate impurities as prescribed by Dutrizac and then subsequently washed with hot water.[15] The Pb-jarosite powder was dried at 80 °C under vacuum for 12 h.

After drying, the jarosite powders were dry ball-milled in polyethylene containers with 500 4 mm hardened 440C stainless steel balls for 72 h at a speed of approximately 80 rpm.

2.2. Physical Characterization. The crystal structures of Na-jarosite and Pb-jarosite powders were characterized with X-ray diffraction (XRD) using a Bruker D8 Focus with a Cu X-ray source with a nickel filter. Ex situ XRD of cycled batteries was performed by the same method. Particle sizes of the jarosite powders were determined using a HORIBA LA-950 particle size analyzer. The relative concentrations of the Na, Pb, and Fe elements of synthesized powders were determined using inductively coupled plasma−optical emission spectroscopy (ICP−OES) with a PerkinElmer Optima 8300. Scanning electron microscopy (SEM) images of jarosite powders were taken on a Sirion XL30. Ex situ Fourier transform infrared (FTIR) spectroscopy was performed on pristine and cycled electrodes using the attenuated total reflectance mode on a Bruker VERTEX 70 FTIR.

2.3. Electrochemical Characterization. Cathodes were prepared from jarosite powders by making a slurry of 70% active material, 20% Super P carbon powder, and 10% carboxymethyl cellulose binder in water. The slurry was deposited onto an aluminum foil current collector via doctor blading and allowed to slowly dry at room temperature before drying under vacuum for 12 h at 80 °C. Jarosite half-cell batteries were assembled in CR2016-type coin cells with commercial lithium metal anodes (MTI Corp.) and a Celgard polypropylene−polyethylene separator inside of an argon-filled glovebox with oxygen and water concentrations below 0.5 ppm. The electrolyte used was a commercial solution of 1 mol L^{-1} $LiPF_6$ in ethylene carbonate (EC) and diethyl carbonate (DEC) in a 1:1 volume ratio (Sigma-Aldrich). The assembled batteries rested for at least 12 h before electrochemical tests.

Galvanostatic cycling was performed between 2.0 and 4.0 V versus Li^+/Li at rates between C/20 and 1C with respect to their theoretical capacities. Cyclic voltammetry was performed on batteries at 0.1 mV/s between 1.6 and 4.0 V. Electrochemical impedance spectroscopy (EIS) was performed on a Solartron instrument between 100 kHz and 0.1 Hz at an amplitude of 5 mV. The potentiostatic intermittent titration technique (PITT) was performed from 4.0 to 2.0 V at 5 mV potential steps until the current decayed below C/200. PITT was preceded by two constant current−constant voltage (CCCV) cycles with a constant current of C/20 and held at 2.0 and 4.0 V until the current dropped below C/200.

3. RESULTS AND DISCUSSION

3.1. Structure and Stoichiometry. XRD peaks of synthesized jarosite powders fit the rhombohedral $R\bar{3}m$ jarosite crystal structure, as indicated by their matching PDFs (Figure 1). $PbSO_4$ impurities were absent from Pb-jarosite after washing with a 10% ammonium acetate solution. Pb-jarosite has a larger lattice spacing of 16.86 Å compared to 16.62 Å for Na-jarosite, as determined by their (006) peak positions. The expanded lattice is likely due to the larger radii of Pb^{2+} ions compared to Na^+. Loss of coulombic attractive forces between $[Fe_3(SO_4)_2(OH)_6]$ layers due to cation vacancies may also contribute to lattice expansion. The slight differences in peak intensity observed between Pb-jarosite and its reference could be caused by differences in composition; for example, it is typical for synthetic jarosites to form solid solutions with hydronium-jarosite.[16,17]

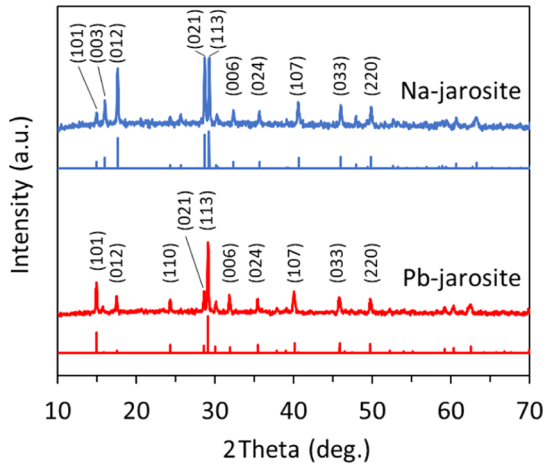

Figure 1. XRD patterns of as-synthesized Na-jarosite and Pb-jarosite samples compared against PDF card nos. 04-015-8168 and 00-033-0759 for natrojarosite and plumbojarosite with selected peaks indexed.

https://dx.doi.org/10.1021/acsaem.0c02762
ACS Appl. Energy Mater. 2021, 4, 2248−2256

ICP−OES analysis determined the metal cation ratio between Na, Pb, and Fe to be 0.54:0:3 and 0:0.33:3 for Na-jarosite and Pb-jarosite, respectively. Charge compensation for missing metal cations could be made possible by crystalline H_3O^+ ions that can form solid solutions in the A-sites of Na-jarosite and Pb-jarosite.[16,17] Additionally, the divalent Pb^{2+} substitution for monovalent Na^+ sites will introduce vacancies in the Pb-jarosite crystal. The resulting chemical formulae based on ICP−OES assuming no Fe^{3+} or anion vacancies are $[Na_{0.54},(H_3O)_{0.46}]Fe_3(SO_4)_2(OH)_6$ and $[Pb_{0.33},(H_3O)_{0.33},\square_{0.33}]Fe_3(SO_4)_2(OH)_6$, where $\square$ represents vacant sites. These results indicate that one-third of 12-coordinate A-sites are vacant in Pb-jarosite.

Laser particle size analysis and SEM of samples after ball milling reveal bulk jarosite powders with average particle sizes of 0.6 and 0.8 μm for Na-jarosite and Pb-jarosite, respectively (Figure 2). The refractive indices used by the particle size analyzer to measure the particle size were 1.83 and 1.88 for Na-jarosite and Pb-jarosite, respectively.[18] These values from the literature were measured for natural natrojarosite and plumbojarosite, which may differ from synthetic analogues which could vary these results.

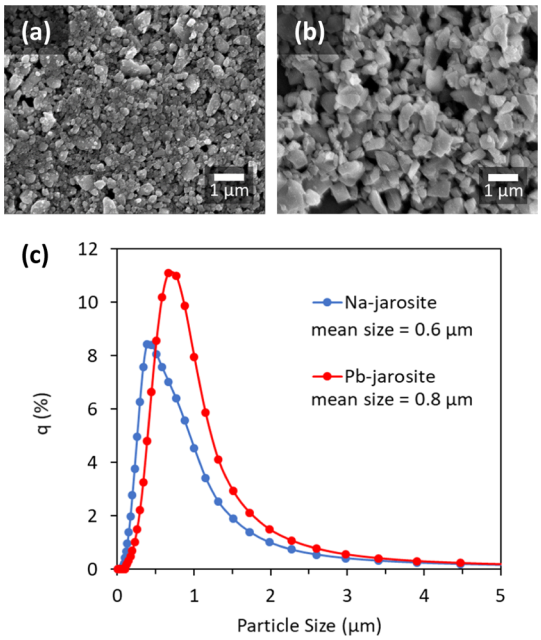

Figure 2. SEM micrograph of Na-jarosite (a) and Pb-jarosite (b) after ball milling. Particle size analysis of synthesized Na-jarosite and Pb-jarosite after ball milling (c).

3.2. Reduction/Oxidation Response. Cyclic voltammetry (CV) of lithium half-cells at 0.1 mV/s shows reduction peaks during the first cycle around 2.4 V for Na-jarosite and at 2.3 V and 2.5 V for Pb-jarosite (Figure 3), corresponding to lithium-ion intercalation and Fe^{3+} reduction. This is followed by oxidation peaks at around 3.0 and 2.6 V for Na-jarosite and Pb-jarosite, respectively. The redox potential is influenced by the local chemical environment of the $Fe^{3+/2+}$ ion as well as site energy of the intercalant ion. Pb has a significantly higher electronegativity than Na (1.9 vs 0.9), and the divalent Pb^{2+} ion will exhibit a larger coulombic force than monovalent Na^+ ions. These elemental properties of Pb may draw more electron density away from neighboring oxygen ions that coordinate to $Fe^{3+/2+}$ centers, thereby increasing the reduction potential of Fe^{3+} via the inductive effect.[19]

The reduction peaks of Na-jarosite become broader and shift in redox potential upon subsequent cycles. Changing redox potential implies a changing environment of the redox active species. Na-jarosite has previously been shown to undergo a change in phase to an amorphous polymeric structure during lithium-ion intercalation.[6] Broadening of CV peaks could be attributed to amorphization, resulting in a range of energy states for lithium-ion insertion.[20] In contrast, the distinct redox peaks present in Pb-jarosite are indicative of a more defined chemical environment, implying a more rigid crystalline host structure upon intercalation. Additionally, a third reduction peak emerges at 2.63 V, which may have been suppressed in the first cycle. The multiple reduction peaks of Pb-jarosite could arise from multiple non-equivalent Fe^{3+} centers or distinct intercalation sites for lithium ions created by the introduction of vacant sites to the crystal structure.

3.3. Galvanostatic Stability. Galvanostatic cycling was performed on batteries at a current rate of C/5 (Figure 4). The specific capacities of the first discharge were 89.8 and 91.4 mA h/g, which correspond to 1.62 and 1.93 Li^+ intercalated per formula unit for Na-jarosite and Pb-jarosite, respectively. This illustrates increased lithium-ion capacity in Pb-jarosite, leading to greater specific capacity despite the increased molecular weight. The increased lithium-ion capacity in Pb-jarosite could be connected to the vacancies introduced in the crystal lattice

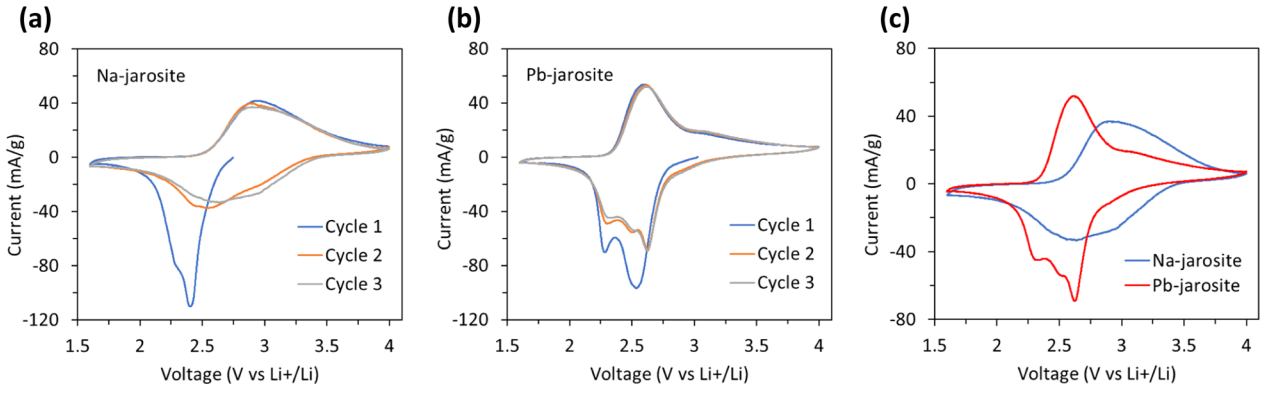

Figure 3. Cyclic voltammetry of Na-jarosite (a), Pb-jarosite (b), and the overlayed third cycle (c) at 0.1 mV/s in coin cells with the lithium metal anode and 1 mol L^{-1} $LiPF_6$ in the EC/DEC electrolyte.

https://dx.doi.org/10.1021/acsaem.0c02762
ACS Appl. Energy Mater. 2021, 4, 2248−2256

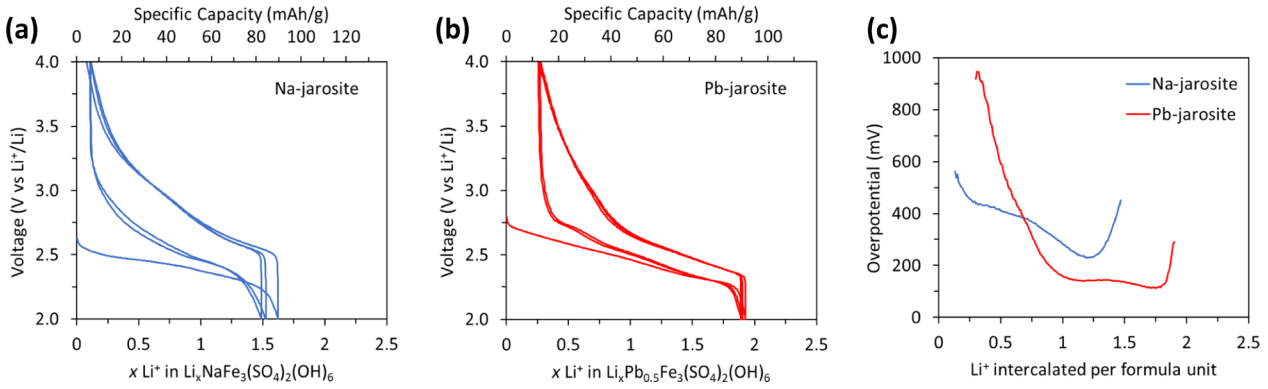

Figure 4. Galvanostatic cycling curves of the first three cycles at C/5 for (a) Na-jarosite and (b) Pb-jarosite. Overpotential between discharge and charge curves of the third cycle (c).

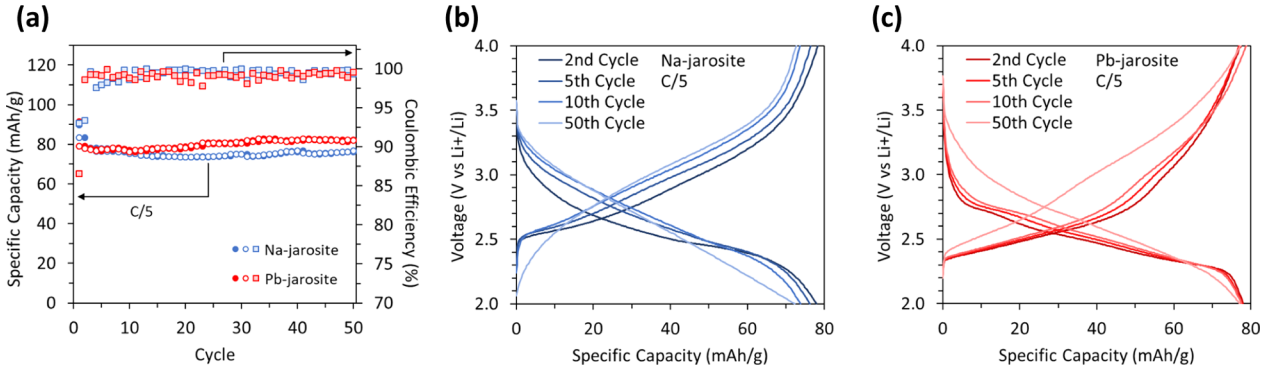

Figure 5. Galvanostatic cycling stability at C/5 for Na-jarosite and Pb-jarosite (a). Closed circles are discharge capacities, open circles are charge capacities, and squares are coulombic efficiencies. Galvanostatic cycling curves at C/5 for Na-jarosite (b) and Pb-jarosite (c) at various cycles.

and larger interplanar spacing between $[Fe_3(SO_4)_2(OH)_6]$ layers, both contributing toward a higher lithium-ion diffusion coefficient. Furthermore, the overpotential is approximated for the third cycle by taking the difference in voltage between charge and discharge curves (Figure 4c). The lower overpotential of Pb-jarosite at lithium concentrations greater than 0.75 indicates better intercalation kinetics and reversibility, which corroborates the small peak-to-peak separation seen in Figure 3b. The changes in overpotential may be related to different intercalation or diffusion mechanisms that vary with concentration and potential. It has been shown that Na-jarosite undergoes a semireversible crystalline-to-amorphous phase transformation upon lithium intercalation.[6,13]

Both materials exhibit capacity loss after the first cycle, possibly due to irreversible intercalation of Li^+ remaining in the host crystal. Pb-jarosite has a larger irreversible loss, as illustrated in Figure 4b, recovering only 86% of its initial capacity compared to 93% for Na-jarosite. Despite lower coulombic efficiency during its first cycle, Pb-jarosite still retained a greater reversible lithium-ion extraction of about 1.6 Li^+/f.u. compared to 1.4 Li^+/f.u. in Na-jarosite at a current rate of C/5.

Furthermore, the cyclic stability is higher in Pb-jarosite, retaining 90.2% of its original capacity compared to 85.0% for Na-jarosite after 50 cycles at a current of C/5 (Figure 5a). However, the galvanostatic voltage profiles significantly change for both materials upon subsequent cycling (Figure 5b,c). With each cycle, the voltage profile loses its typical plateau shape and becomes more linear. This trend matches the broadening of redox peaks in CV for Na-jarosite and indicates a more solid-solution-like intercalation behavior. Additionally, CV of batteries after galvanostatic cycling generated voltammograms with broad profiles and attenuated redox peaks (Figure 6). It is

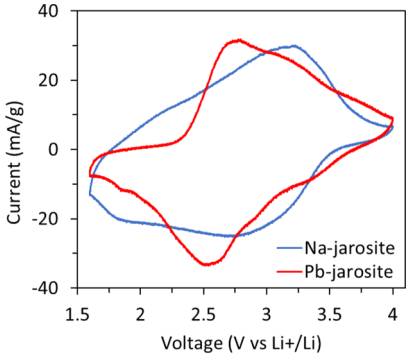

Figure 6. Cyclic voltammetry of Na- and Pb-jarosite after cycling.

evident from the transformation of voltage profiles that the local environment of the $Fe^{3+/2+}$ redox center irreversibly changes during cycling. The linear galvanostatic profile and pseudo-capacitive-like voltammogram of Na-jarosite resembles the intercalation chemistry of other amorphous materials.[20] This is due to the distribution of energies created by the disordered ligand environment and intercalation sites.

3.4. Electrochemical Induced Phase Transformation.

It has been illustrated by Gnanavel et al. that Na-jarosite undergoes a reversible crystalline-to-amorphous phase transformation upon lithium intercalation and deintercalation, suggesting that the amorphous phase is closely related in

https://dx.doi.org/10.1021/acsaem.0c02762
ACS Appl. Energy Mater. 2021, 4, 2248−2256

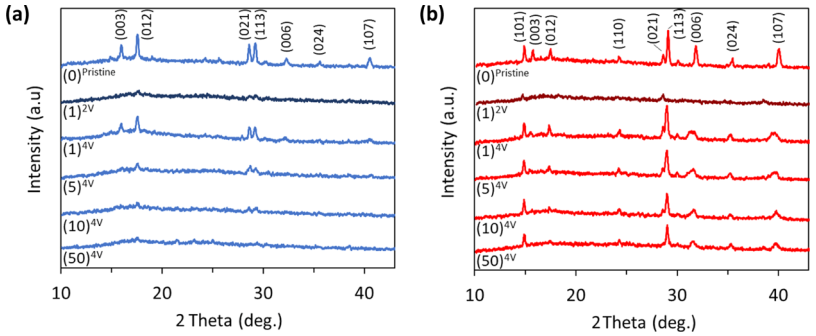

Figure 7. Ex situ XRD patterns of Na-jarosite (a) and Pb-jarosite (b) electrodes at various cycles.

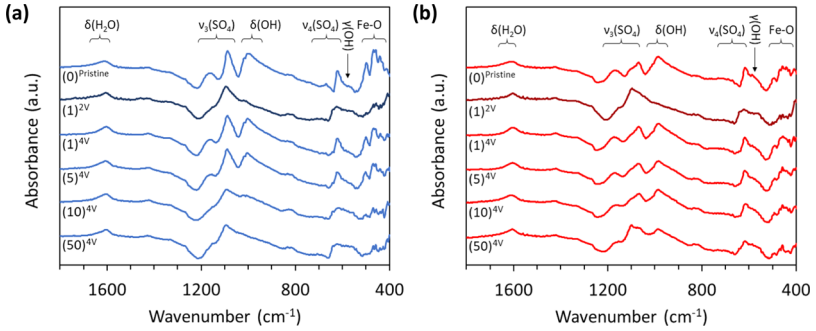

Figure 8. Ex situ FTIR spectra of pristine and cycled Na-jarosite (a) and Pb-jarosite (b) electrodes.

structure to crystalline jarosite.[6] However, the longevity of this reversible transformation was not investigated. Recently, Kosova et al. reported irreversible amorphization of Na-jarosite and attributed it to the low structural stability of a Na/Li intermediate phase due to Li substitution during cycling.[13]

To further understand how the jarosite structure changes during cycling, ex situ XRD was performed on cycled electrodes (Figure 7). Both Na-jarosite and Pb-jarosite undergo a crystalline-to-amorphous transformation during their first discharge to 2.0 V evidenced by diminished diffraction peaks. Recharging to 4.0 V coincides with the regaining of periodic order of the crystal structure, illustrating the reversible transformation between amorphous and crystalline phases via electrochemical intercalation and deintercalation.

Another observation to make is the disproportional decrease in intensity and broadening after the first charge cycle of the (003), (006), and (107) peaks in Pb-jarosite. The changes of these particular peaks indicate a loss in periodicity of the interlayer crystallographic direction, while the intralayer directions better retain the long-range order. This helps support the Gnanavel et al. hypothesis that jarosite undergoes a topotactic transformation into a non-periodic layered structure.[6]

In agreement with Kosova's findings, the phase transformation loses reversibility upon further cycling. By the 50th charge cycle, Na-jarosite has nearly lost all diffraction peaks, while Pb-jarosite still retains its strongest peaks, albeit at lower intensity. The gradual amorphization corroborates the evolving voltage profiles during galvanostatic cycling which occurs to a greater extent in Na-jarosite.

The ability for Pb-jarosite to better revert back to its crystalline structure may be evidence of a more stable crystal structure compared to Na-jarosite and less prone to Li-ion substitution, as described by Kosova.[13] Pb^{2+} and Na^{+} ions reside in the interstitials of large 12-coordinate oxygen icosahedron cages. The stability of ionic polyhedra generally follows the cation−anion radius ratio limits according to Pauling's rules for ionic crystals, with the critical radius ratio of 12-coordinate polyhedra being 1. Considering the Shannon ionic radii for 12-coordinate Pb^{2+} and Na^{+}, 1.49 and 1.39 Å, respectively, and 1.40 Å for O^{2-}, the cation−anion ratios are 1.06 and 0.99 for Pb^{2+} and Na^{+}, respectively.[21] This illustrates that Pb^{2+} would be the more stable cation in the jarosite structure and could be explanation for Pb-jarosite's improved reversion to its crystalline form upon deintercalation. Furthermore, Pb^{2+} would be less susceptible to deintercalation and Li^{+} substitution due to its larger size and stronger coulombic interactions. However, the Pb-jarosite sample may also contain H_3O^{+} ions which are similar in size to Na^{+} and would be more susceptible to ion exchange. Therefore, the crystal may undergo structural change due to Li/H_3O exchange but still retain some crystallinity after many cycles in comparison to Na-jarosite.

Ex situ FTIR further corroborates the local structural changes of jarosite during cycling (Figure 8). Absorption spectra of uncycled electrodes agree with those from the literature.[6,13,22,23] The absorption bands between 400 and 520 cm^{-1} are attributed to Fe−O. Bands around 620−670 and 1080−1170 cm^{-1} correspond to the ν_4 and ν_3 vibration modes of SO_4^{2-}, respectively. Absorption bands near 1000 cm^{-1} correspond to bending δ(OH) groups, while the shoulder band at 570 cm^{-1} may be ascribed to the γ(OH) vibration mode.[23] Additionally, the band near 1620 cm^{-1} is the water-bending $\delta(H_2O)$ vibration which corroborates the presence of H_3O^{+} substituted in A-sites accounting for missing Na^{+} and Pb^{2+} from ICP−OES results.[22]

In agreement with the literature investigating the local structure of jarosite during lithium intercalation, the FTIR spectra of reduced Na-jarosite and Pb-jarosite after its first

https://dx.doi.org/10.1021/acsaem.0c02762
ACS Appl. Energy Mater. 2021, 4, 2248−2256

discharge to 2 V display decreased Fe−O and δ(OH) band intensity and blue shift of the ν_4 and ν_3 vibration modes of sulfate groups.[6,13] Furthermore, upon delithiation, both Na-jarosite and Pb-jarosite nearly revert back to their original structures. Gnanavel et al. hypothesized that the decrease in Fe−O band intensity was caused by breaking of Fe−O−S bonds and creation of FeO_5 polyhedra during lithium-ion interaction. However, Kosova et al. were unable to confirm the presence of FeO_5 polyhedra in lithiated Na-jarosite through Mössbauer spectroscopy in comparison to other FeO_5 compounds in the literature.[13] Nonetheless, subsequent cycling of both Na-jarosite and Pb-jarosite results in irreversible distortion of the jarosite structure, as evidenced by its FTIR spectra and XRD pattern.

The transformation of the local structure corroborates the evolving voltage profiles during galvanostatic cycling and cyclic voltammetry which occurs to a greater extent in Na-jarosite. A changing redox potential is indicative of a changing local chemical environment surrounding the $Fe^{3+/2+}$ redox centers which is related to the energy levels of d-orbitals in Fe ions.[24] In the crystalline jarosite phase, all Fe ions should exist in octahedral coordination; however, as the jarosite structure becomes amorphous and Fe−O coordination becomes distorted, there may exist a distribution of energies that give rise to the linear sloping galvanostatic profile. The same effect is observed for Na-ion intercalation of amorphous V_2O_5 compared to crystalline.[20]

3.5. Kinetics of Na-Jarosite and Pb-Jarosite. Pb-jarosite and Na-jarosite batteries were cycled at different C-rates to investigate the influence of lithium-ion kinetics (Figure 9). Na-

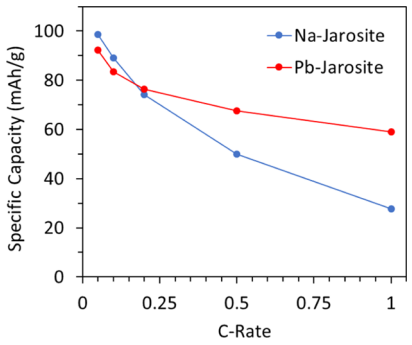

Figure 9. Discharge capacities of Na-jarosite and Pb-jarosite at different C-rates.

jarosite displayed greater lithium-ion capacity at lower current rates but had more significant capacity drop-off at higher rates than Pb-jarosite. At slow currents, it would be expected that Na-jarosite has higher capacity because of its higher theoretical specific capacity. Conversely, Pb-jarosite had a superior capacity of 59 mA h/g at 1C compared to 28 mA h/g for Na-jarosite. The larger dependence on C-rate is indicative of more kinetically restricted behavior. The improved reaction kinetics of Pb-jarosite could be indicative of improved electronic properties and lithium-ion diffusivity.

EIS of Na-jarosite and Pb-jarosite batteries further illustrates the improved kinetics of Pb-jarosite (Figure 10). EIS spectra show that Pb-jarosite has a smaller charge-transfer resistance indicated by the lower x-intercept of the large semicircle. Improved charge transfer could result from better electronic properties by substituting Pb for Na ions and introducing

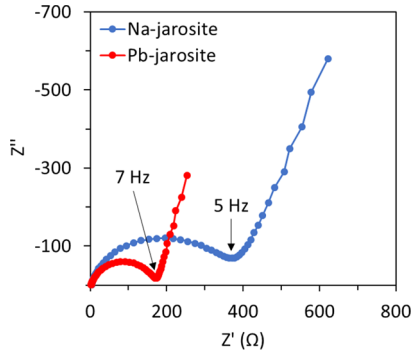

Figure 10. EIS spectra between 100 kHz and 0.1 Hz of lithium half-cell batteries before cycling.

vacancies. A lower charge-transfer resistance would help contribute to better rate performance of Pb-jarosite.

Furthermore, the low-frequency Warburg region of EIS spectra pertains to lithium-ion diffusion. The lithium-ion diffusion coefficient (D_{Li^+}) can be calculated using the following methodology proposed by Ho et al.

$$D_{Li^+} = \frac{1}{2}\left[\left(\frac{V_M}{AF\sigma_W}\right)\frac{\delta E}{\delta x}\right]^2 \quad (1)$$

where V_M is the molar volume, A is the electrode/electrolyte surface area (simplified as the electrode area, 0.785 cm^2), F is the Faraday constant, and σ_W is the Warburg coefficient, which is determined from the slope of real impedance Z' versus the inverse square root of angular frequency $\omega^{-1/2}$ at low frequencies.[25] The parameter $\delta E/\delta x$ is estimated from the first plateau of the galvanostatic test in Figure 4 as the change in potential versus lithium-ion insertion. The resulting diffusion coefficients are 4.3×10^{-13} and 1.7×10^{-11} cm^2 s^{-1} for Na-jarosite and Pb-jarosite, respectively, thus showing Pb-jarosite to have 2 orders of magnitude faster diffusion. It should be noted that these are only nominal values due to the assumptions made about the electrode/electrolyte interface, but the comparison should still be considered appropriate.

PITT further corroborated the relationship of the lithium-ion diffusion in Na-jarosite and Pb-jarosite. PITT measured the potentiostatic current response at 5 mV steps starting from 4 V (Figure S1). The decay in current during a potentiostatic test can be modeled by the Cottrell equation to determine kinetic parameters such as diffusion coefficient. A fitting approximation developed by Vorotyntsev et al. was used.[26] At early times when diffusion dominates the kinetics, the current is described by

$$I(t_{short}) = \frac{Q^{total}}{\tau_D/\Lambda + \sqrt{\pi\tau_D t}} \quad (2)$$

where Q^{total} is the total capacity per voltage increment, t is the time, τ_D is the characteristic diffusion time which is equal to L^2/D, where L is the characteristic particle size and D is the diffusion coefficient, and Λ is the ratio of the diffusion resistance to the external resistance. The parameters τ_D and Λ are determined graphically by finding the slope and intercept of the linear regression of $1/(I(t)\sqrt{t})$ versus $1/\sqrt{t}$ at early times

$$m = \frac{\tau_D}{\Lambda Q^{total}} \quad (3)$$

https://dx.doi.org/10.1021/acsaem.0c02762
ACS Appl. Energy Mater. 2021, 4, 2248−2256

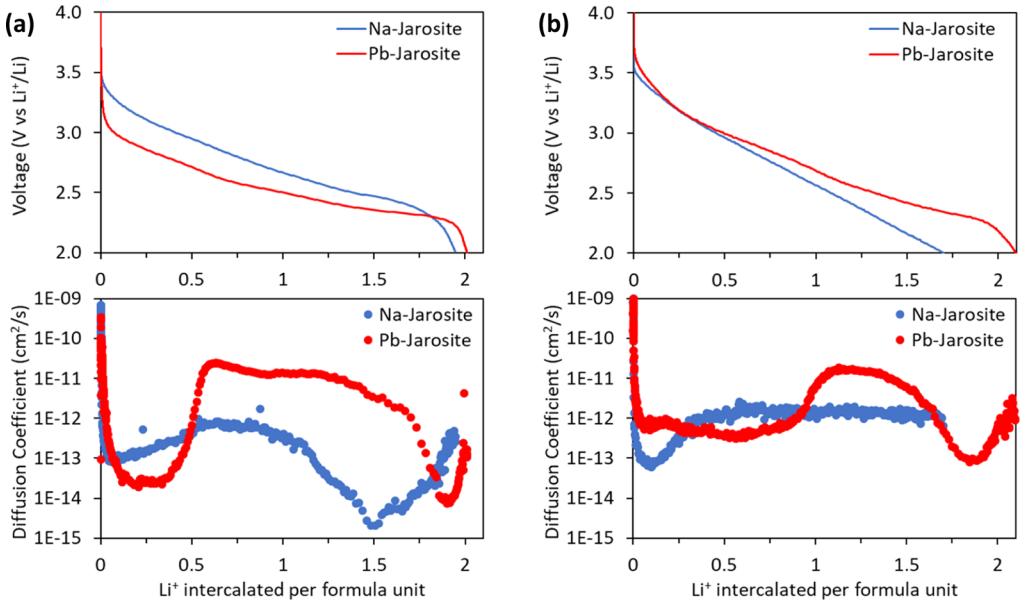

Figure 11. PITT discharge profile and the calculated diffusion coefficient of Na-jarosite and Pb-jarosite before cycling (a) and after 30 galvanostatic cycles at C/5 (b). PITT was preceeded by two CCCV cycles.

$$b = \frac{\sqrt{\pi \tau_D}}{Q^{total}} \tag{4}$$

The parameters τ_D and Λ were found for each potential step and used to calculate the diffusion coefficient (Figure S2).

The calculated diffusion coefficient varies during lithium-ion intercalation in Na-jarosite and Pb-jarosite (Figure 11a). In general, the weighted average diffusion coefficients when considering the amount of lithium intercalated at each potential step are 8.6×10^{-13} and 1.1×10^{-11} cm^2 s^{-1} for Na-jarosite and Pb-jarosite, respectively. The larger average diffusion coefficient over all lithium concentrations corroborates the improved capacity and rate performance of Pb-jarosite over Na-jarosite. However, Pb-jarosite exhibits lower lithium-ion diffusivity than Na-jarosite at lower lithium concentrations but increases to higher diffusivity upon further intercalation. This region of low diffusivity corresponds well with the large overpotential of Pb-jarosite during initial intercalation (Figure 4c).

An explanation to the large change in diffusion coefficient and overpotential in Pb-jarosite could be the transition between lithium intercalation into amorphous Pb-jarosite and its crystalline phase. It has already been shown that both jarosite materials undergo a semireversible crystalline-to-amorphous phase transformation upon lithium intercalation (Figure 7). The PITT test was preceded by two CCCV cycles which would have contributed to the formation of some amorphous Pb-jarosite phase. It could be hypothesized that the trend in diffusivity and overpotential during the third cycle represents initial lithium-ion intercalation into the amorphous phase at high potential, followed by intercalation into the crystalline phase with higher diffusivity, and then the biphasic crystalline-to-amorphous transformation upon further intercalation. The amorphous phase would not receive the same benefits from vacancies due to its disordered structure. Additionally, the lower density of the amorphous phase would result in larger hopping distances for lithium ions, further decreasing diffusivity. In contrast, Na-jarosite without vacancies does not receive the same boost in diffusivity for its crystalline phase.

PITT performed after 30 galvanostatic cycles at C/5 illustrates the growing amorphous environment for lithium diffusion (Figure 11b). Pb-jarosite retains a high diffusivity above 10^{-11} cm^2 s^{-1}, albeit throughout a smaller concentration range. Similarly, the proportion of the low-diffusivity region during initial intercalation increases. In contrast, Na-jarosite exhibits a mostly unchanging diffusion coefficient during intercalation which is consistent with the diffusivity independence on lithium concentration in disordered materials because of less change in the local environment during intercalation.[27] This supports the idea that Na-jarosite and Pb-jarosite are irreversibly transforming into a disordered phase through electrochemical cycling, with Pb-jarosite being more resilient to the irreversible transformation. The decreasing high-diffusivity region could correspond with decreasing crystalline content of Pb-jarosite and increasing amorphous phase that does not receive the same boost in diffusivity from vacancies. These trends in diffusivity are confirmed separately by performing intermittent EIS during discharge of the same cycled batteries (Figure S5).

4. CONCLUSIONS

Lithium-ion intercalation into synthetic Pb-jarosite was investigated and compared to its Na-jarosite analogue. Substituting Pb^{2+} for Na^+ in the synthesis of jarosite results in the formation of cation vacancies that help contribute to lower charge-transfer resistance and improved lithium-ion diffusion. Additionally, the presence of Pb^{2+} mitigated irreversible transformation into the amorphous phase. Despite having a lower theoretical specific capacity, Pb-jarosite demonstrated increased lithium-ion uptake at competitive rates attributed to faster diffusion kinetics and lower charge-transfer resistance. However, average diffusivity in Pb-jarosite decreases during the accumulation of the amorphous phase over several cycles.

This work helps contribute to the understanding of solid ionic diffusion in jarosite materials with unique amorphous

https://dx.doi.org/10.1021/acsaem.0c02762
ACS Appl. Energy Mater. 2021, 4, 2248−2256

phase transformation over many cycles. The characterization of Pb-jarosite having higher lithium-ion diffusivity and capacity helps to open the possibility of recycling jarosite waste materials in energy storage applications. Additionally, it suggests that utilizing mixed jarosite waste materials with a higher Pb content would be more desirable. Although jarosite underperforms compared to commercial lithium-ion battery cathodes, its potential economic advantage may make it suitable for alternative niche battery applications.

■ ASSOCIATED CONTENT

Supporting Information

The Supporting Information is available free of charge at https://pubs.acs.org/doi/10.1021/acsaem.0c02762.

PITT current/voltage profile, graphical transformation of PITT data, intermittent galvanostatic and EIS profiles, and intermittent EIS diffusivity results (PDF)

■ AUTHOR INFORMATION

Corresponding Author

Guozhong Cao − *Department of Materials Science and Engineering, University of Washington, Seattle, Washington 98195, United States;* orcid.org/0000-0001-6539-0490; Email: gzcao@uw.edu

Authors

Zachary G. Neale − *Department of Materials Science and Engineering, University of Washington, Seattle, Washington 98195, United States;* orcid.org/0000-0001-7279-7766

Michael Barta − *Department of Materials Science and Engineering, University of Washington, Seattle, Washington 98195, United States*

Complete contact information is available at: https://pubs.acs.org/10.1021/acsaem.0c02762

Notes

The authors declare no competing financial interest.

■ ACKNOWLEDGMENTS

This work was supported by the National Science Foundation (CBET-1803256).

■ REFERENCES

(1) Dutrizac, J. E.; Jambor, J. L. Jarosites and Their Application in Hydrometallurgy. *Rev. Mineral. Geochem.* **2019**, *40*, 405−452.

(2) Szymanski, J. T. The Crystal Structure of Plumbojarosite Pb[Fe3(SO4)2(OH)6]2. *Can. Mineral.* **1985**, *23*, 659−668.

(3) Karamanov, A.; Taglieri, G.; Pelino, M. Iron-Rich Sintered Glass-Ceramics from Industrial Wastes. *J. Am. Ceram. Soc.* **1999**, *82*, 3012.

(4) Patrick Mubiayi, M.; Elizabeth Makhatha, M.; Titilayo Akinlabi, E. Characterization, Leachate Characteristics and Compressive Strength of Jarosite/Clay/Fly Ash Bricks. *Mater. Today: Proc.* **2018**, *5*, 17802.

(5) Asokan, P.; Saxena, M.; Asolekar, S. R. Hazardous Jarosite Use in Developing Non-Hazardous Product for Engineering Application. *J. Hazard. Mater.* **2006**, *137*, 1589.

(6) Gnanavel, M.; Pralong, V.; Lebedev, O. I.; Caignaert, V.; Bazin, P.; Raveau, B. Lithium Intercalation into the Jarosite-Type Hydroxysulfate: A Topotactic Reversible Reaction from a Crystalline Phase to an Inorganic Polymer-like Structure. *Chem. Mater.* **2014**, *26*, 4521.

(7) Gnanavel, M.; Lebedev, O. I.; Bazin, P.; Raveau, B.; Pralong, V. Reversible Transformation from Amorphouse Na3Fe3(SO4)2(OH)6 to Crystallized NaFe3(SO4)2(OH)6 Jarosite-Type Hydroxysulfate. *Solid State Ionics* **2015**, *278*, 38−42.

(8) Ding, Y.-L.; Wen, Y.; Van Aken, P. A.; Yu, Y.; Yu, Y. Jarosite Nanosheets Fabricated via Room-Temperature Synthesis as Cathode Materials for High-Rate Lithium Ion Batteries. *Chem. Mater.* **2015**, *27*, 3143−3149.

(9) Ding, Y.-L.; Wen, Y.; Chen, C.-C.; Van Aken, P. A.; Yu, Y.; Yu, Y. Nanosheets of Earth-Abundant Jarosite as Novel Anodes for High-Rate and Long-Life Lithium-Ion Batteries. *ACS Appl. Mater. Interfaces* **2015**, *7*, 10518−10524.

(10) Xu, W.; Xie, Z.; Cui, X.; Zhao, K.; Zhang, L.; Mai, L.; Wang, Y. Direct Growth of an Economic Green Energy Storage Material: A Monocrystalline Jarosite-KFe3(SO4)2(OH)6-Nanoplates@rGO Hybrid as a Superior Lithium-Ion Battery Cathode. *J. Mater. Chem. A* **2016**, *4*, 3735.

(11) Zhao, R.; Li, Y.; Chan, C. K. Synthesis of Jarosite and Vanadium Jarosite Analogues Using Microwave Hydrothermal Reaction and Evaluation of Composition-Dependent Electrochemical Properties. *J. Phys. Chem. C* **2016**, *120*, 9702−9712.

(12) Sandineni, P.; Yaghoobnejad Asl, H.; Choudhury, A. Kagomé Lattices as Cathode: Effect of Particle Size and Fluoride Substitution on Electrochemical Lithium Insertion in Sodium- and Ammonium Jarosites. *J. Solid State Chem.* **2016**, *242*, 78.

(13) Kosova, N. V.; Shindrov, A. A.; Kabanov, A. A. Theoretical and Experimental Study of Reversible Intercalation of Li Ions in the Jarosite NaFe3(SO4)2(OH)6 Structure. *Electrochim. Acta* **2020**, *359*, 136950.

(14) Dutrizac, J. E. Factors Affecting Alkali Jarosite Precipitation. *Metall. Trans. B* **1983**, *14*, 531.

(15) Dutrizac, J. E.; Dinardo, O.; Kaiman, S. Factors Affecting Lead Jarosite Formation. *Hydrometallurgy* **1980**, *5*, 305.

(16) Basciano, L. C.; Peterson, R. C. Jarosite-Hydronium Jarosite Solid-Solution Series with Full Iron Site Occupancy: Mineralogy and Crystal Chemistry. *Am. Mineral.* **2007**, *92*, 1464.

(17) Jambor, J. L.; Dutrizac, J. L. The Synthesis of Beaverite. *Can. Mineral.* **1985**, *23*, 47−51.

(18) Fleischer, M.; Wilcox, R. E.; Matzko, J. J. MICROSCOPIC DETERMINATION OF THE NONOPAQUE MINERALS. *Microscopic Determination of the Nonopaque Minerals*; US Government Printing Office, 1984

(19) Gutierrez, A.; Benedek, N. A.; Manthiram, A. Crystal-Chemical Guide for Understanding Redox Energy Variations of M 2+/3+ Couples in Polyanion Cathodes for Lithium-Ion Batteries. *Chem. Mater.* **2013**, *25*, 4010−4016.

(20) Uchaker, E.; Zheng, Y. Z.; Li, S.; Candelaria, S. L.; Hu, S.; Cao, G. Z. Better than Crystalline: Amorphous Vanadium Oxide for Sodium-Ion Batteries. *J. Mater. Chem. A* **2014**, *2*, 18208−18214.

(21) Shannon, R. D. Revised Effective Ionic Radii and Systematic Studies of Interatomic Distances in Halides and Chalcogenides. *Acta Crystallogr., Sect. A: Cryst. Phys., Diffr., Theor. Gen. Crystallogr.* **1976**, *32*, 751.

(22) Basciano, L. C.; Peterson, R. C. Crystal Chemistry of the Natrojarosite-Jarosite and Natrojarosite-Hydronium Jarosite Solid-Solution Series: A Synthetic Study with Full Fe Site Occupancy. *Am. Mineral.* **2008**, *93*, 853−862.

(23) Bishop, J. L.; Murad, E. The Visible and Infrared Spectral Properties of Jarosite and Alunite. *Am. Mineral.* **2005**, *90*, 1100−1107.

(24) Liu, C.; Neale, Z. G.; Cao, G. Understanding Electrochemical Potentials of Cathode Materials in Rechargeable Batteries. *Mater. Today* **2016**, *19*, 109−123.

(25) Ho, C.; Raistrick, I. D.; Huggins, R. A. Application of A-C Techniques to the Study of Lithium Diffusion in Tungsten Trioxide Thin Films. *J. Electrochem. Soc.* **1980**, *127*, 343.

(26) Vorotyntsev, M. A.; Levi, M. D.; Aurbach, D. Spatially Limited Diffusion Coupled with Ohmic Potential Drop and/or Slow Interfacial Exchange: A New Method to Determine the Diffusion Time Constant and External Resistance from Potential Step (PITT) Experiments. *J. Electroanal. Chem.* **2004**, *572*, 299.

(27) Lee, J.; Urban, A.; Li, X.; Su, D.; Hautier, G.; Ceder, G. Unlocking the Potential of Cation-Disordered Oxides for Rechargeable Lithium Batteries. *Science* **2014**, *343*, 519−522.

https://dx.doi.org/10.1021/acsaem.0c02762
ACS Appl. Energy Mater. 2021, 4, 2248−2256